




**Tunneling magnetoresistance and spin-valley polarization in magnetic silicene superlattices**J. G. Rojas-Briseño  and M. A. Flores-Carranza*Unidad Académica de Física, Universidad Autónoma de Zacatecas, Calzada Solidaridad Esquina con Paseo la Bufa S/N, 98060 Zacatecas, Zacatecas, Mexico*P. Villasana-Mercado , S. Molina-Valdovinos , and I. Rodríguez-Vargas \**Unidad Académica de Ciencia y Tecnología de la Luz y la Materia, Universidad Autónoma de Zacatecas, Carretera Zacatecas-Guadalajara Km. 6, Ejido La Escondida, 98160 Zacatecas, Zacatecas, Mexico* (Received 7 January 2021; revised 17 April 2021; accepted 19 April 2021; published 28 April 2021)

We study the tunneling magnetoresistance and the spin-valley transport in silicene-based magnetic superlattices. The superlattice profile is obtained by the periodic modulation of the exchange field induced by ferromagnetic electrodes. The silicene band gap in the superlattice structure is also modulated through an external perpendicular electric field. The concept of parallel and antiparallel magnetization configurations of single magnetic junctions is extended to the periodic case by switching the magnetization orientation of the adjacent magnetic barriers in parallel and antiparallel fashion. The transfer matrix method and the Landauer-Büttiker formalism are used to obtain the transmission and transport properties, respectively. We find an oscillating conductance once the periodic modulation is incorporated. By tuning the external perpendicular electric field a conductance gap is obtained for the antiparallel configuration, which results in an enhancement of the tunneling magnetoresistance with respect to single magnetic junctions. In the case of the spin-valley polarization it is not possible to obtain two well-defined polarization states by simply switching the magnetization orientation, as in single magnetic junctions, due to the equivalence of the spin-valley conductance components. However, by inducing structural asymmetry in the width of barriers-wells, two well-defined polarization states can be reached. Moreover, an additional enhancement of the tunneling magnetoresistance is induced by the structural asymmetry. Our findings indicate that magnetic periodic modulation can be an option to improve the tunneling magnetoresistance and the spin-valley polarization of silicene-based structures.

DOI: [10.1103/PhysRevB.103.155431](https://doi.org/10.1103/PhysRevB.103.155431)**I. INTRODUCTION**

The multiple degrees of freedom of two-dimensional (2D) materials are ideal for versatile multifunctional devices. In particular, the spin and valley degrees of freedom raise the prospects of spintronics and valleytronics [1–3]. For instance, the long diffusion length, the lifetime, and the compatibility with other 2D materials, including ferromagnets, make graphene ideal as a spin transport channel material. The graphene's low spin-orbit coupling (SOC) and the high carrier mobility can enhance the spin coherence length as well as the spin diffusive transport. In fact, it has been reported that spin signals can be transported up to 35.5  $\mu\text{m}$  and even up to 90  $\mu\text{m}$  using carrier drift [4,5]. Another important factor is the so-called spin injection efficiency, that is, the injection of a well-polarized current from a ferromagnetic electrode to the graphene transport channel. Actually, since the first demonstration of spin transport in graphene [6], the spin injection efficiency has been improved systematically, reaching values of up to 60% [7]. In the case of valleytronics, significant progress has been made since the first demonstration of valley polarization in 2D materials [8]. Nowadays, it is

possible to achieve valley polarization by valley-selective circular dichroism [8], optical pumping techniques [9,10], and electrical methods [11,12]. The 2D material *par excellence* for valley polarization so far has been  $\text{MoS}_2$ , owing to its intrinsic characteristics such as inequivalent valleys, strong SOC, and lack of inversion symmetry. However, other 2D materials with inequivalent valleys are also candidates for valleytronics. Recently, the state of the art of spintronics and valleytronics has been well documented in excellent reviews [1–3]. Another important breakthrough that can advance significantly the field of spin-valleytronics is the integration of 2D materials with materials with intrinsic magnetic properties. In fact, recently graphene has been integrated with antiferromagnetic CrSe, resulting in an exchange splitting of about 134 meV [13]. So, we can think about manipulating spin-valley degrees of freedom by placing 2D materials close to ferromagnets, ferrimagnets, and antiferromagnets.

Under this context, the door is open for other 2D materials that meet the fundamental requirements for spin-valleytronics. Such is the case of silicene [14–16], a 2D material with two inequivalent valleys, significant SOC [17], and a local band gap (on-site potential) [17,18] modulable via gating [19,20]. Since 2012 there is experimental evidence of its fabrication by epitaxial growth on metallic substrates [21–23], and in 2015 its integration in device geometries was possible [24].

\*isaac@uaz.edu.mx

Furthermore, novel phenomena such as the spin Hall effect [17], the quantum anomalous Hall effect [25], the valley-polarized quantum Hall effect [26], topological superconductivity [27], and the bipolar spin-valley diode effect [28] have been reported.

In silicene the spin and valley are coupled and can give rise to spin currents generated in each valley with opposite polarities. The silicene's electron spin has a long relaxation time and a long coherence length [29,30]. To induce spin-valley-polarized currents, we need to break the valley and/or time-reversal symmetry [31,32]. The valley asymmetry gives rise to fundamental differences in the electronic states, resulting in effective valley polarization [25,26,28]. Magnetoresistance is another quantity of great technological relevance that has attracted a lot of interest in silicene due to the giant values reported in silicene nanoribbons [33] and silicene with ferromagnetic gates [34]. For the latter, the stray field associated with the ferromagnetic gates induces wave vector filtering that results in substantial differences in the transport properties of the parallel and antiparallel magnetization configurations, giving rise to giant tunneling magnetoresistance. In principle, the modulation of silicene's band structure allows us to control the spin-valley degrees of freedom as well as to enhance the magnetoresistance response. Thus we can think about multifunctional silicene-based devices with spin-valley polarization and magnetoresistive capabilities. For instance, in single magnetic tunnel junctions it is possible to achieve 100% spin-valley polarization and a tunneling magnetoresistance response with percents of hundreds to thousands by modulating the exchange field strength and the on-site potential [35]. Moreover, the 100% positive-negative spin-valley polarization states are accessible by simply switching the magnetization configuration. As far as we know, there are few works dealing with these multifunctional silicene structures [35–38]. Most of the proposals focus on the optimization of the spin-valley polarization. In fact, several strategies were proposed such as gating [39–46], strain [47–50], Fermi velocity barriers [51–53], magnetic barriers, and ferromagnetic junctions [54–64]. In the case of the tunneling magnetoresistance, similar structures were assessed [65–68]. However, in this case the parallel and antiparallel magnetization configurations are always in play. Of particular interest are superlattices owing to the possible optimization of the spin-valley polarization [44–46,49,50,53,59–64] and the enhancement of the tunneling magnetoresistance [67,68]. The periodic modulation results in oscillating transport properties with significant differences in the spin-valley components or the magnetization configurations. In this context, we consider that a thorough assessment of versatile silicene superlattices with spin-valley polarization and tunneling magnetoresistance capabilities is necessary.

Here, we show that by extending the concept of the magnetic tunnel junction to the periodic case, which from now on we refer to as magnetic silicene superlattices (MSSLs), it is possible to improve the silicene's tunneling magnetoresistance response significantly as well as to obtain two well-defined spin-valley polarization states. Specifically, we find that the periodic magnetic modulation induces oscillations in the transport and transport-related properties: conductance, spin-valley polarization, and tunneling magnetoresistance.

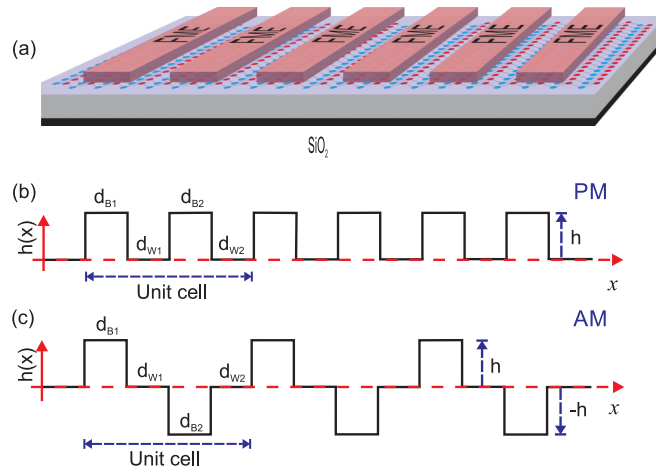


FIG. 1. (a) Schematic representation of magnetic silicene superlattices. Silicene is placed on a supporting substrate such as  $\text{SiO}_2$  and nanostructured with ferromagnetic electrodes in periodic fashion to generate the magnetic superlattice profile. The exchange field profile is shown along the superlattice axis for the (b) parallel and (c) antiparallel magnetization configurations of the system. The superlattice unit cell is composed of two ferromagnetic electrodes (barriers) and two free regions (wells), the second electrode being the soft region of the magnetic superlattice. The parallel and antiparallel magnetization configurations are set by keeping or reversing the magnetization of the soft region.

More importantly, the tunneling magnetoresistance of MSSLs is enhanced with respect to single magnetic tunnel junctions [35]. Furthermore, in order to obtain two well-defined spin-valley polarization states it is necessary to induce structural asymmetry in MSSLs. Structural asymmetry also helps to improve the tunneling magnetoresistance. So, our findings indicate that MSSLs represent an excellent option for versatile devices that demand spin-valley polarization and magnetoresistance capabilities.

The rest of this paper is organized as follows: In Sec. II, the details of MSSLs are presented in conjunction with the theoretical model used to obtain the spin-valley and magnetoresistance transport properties. In Sec. III we show and discuss the most relevant results of symmetric and asymmetric MSSLs. Finally, we summarize our work with the corresponding conclusions in Sec. IV.

## II. THEORETICAL FORMALISM

The system that we are interested in is shown in Fig. 1(a). It consists of a silicene layer placed on a supporting substrate such as  $\text{SiO}_2$  and ferromagnetic electrodes (FMEs) over silicene arranged in periodic fashion to create the so-called MSSLs. A dielectric slab (not shown) is typically placed between silicene and the FMEs to avoid silicene degradation. Two FMEs alternating with two free regions constitute the unit cell of MSSLs, the second FME being the soft region. This region allows us to change the magnetization configuration of our structure. In particular, we can go from parallel (PM) to antiparallel magnetization (AM) configuration by reversing the magnetization direction. The exchange field profile for PM and AM configurations is shown in Figs. 1(b) and 1(c),

respectively. For PM we have a stepwise exchange field profile, while for AM the profile is alternated with positive and negative exchange field regions. A metallic electrode along the superlattice structure and underneath FMEs is used to modulate the silicene on-site potential  $\Delta_z$  (local band gap) through an electric field applied perpendicularly to the silicene. The exchange field strength that results from the magnetic proximity effect of the FMEs is given by  $h$  [69–71], the widths of the magnetic barriers are given by  $d_{B1}$  and  $d_{B2}$ , and the widths of the well (free) regions are given by  $d_{w1}$  and  $d_{w2}$ . The number of superlattice periods  $N$  is given by the number of unit-cell repetitions. For the MSSSLs shown in Fig. 1 we have considered three superlattice periods.

The charge carriers in MSSSLs can be described by the low-energy effective Hamiltonian [17–19,54,72]

$$\hat{H} = v_F(p_x\sigma_x - \tau_z p_y\sigma_y) - (s_z\tau_z\Delta_{so} - \Delta_z(x))\sigma_z - s_z h(x), \quad (1)$$

where

$$\Delta_z(x) = \begin{cases} \Delta_z & \text{for barriers and wells} \\ 0 & \text{otherwise,} \end{cases} \quad (2)$$

and

$$h(x) = \begin{cases} \theta h & \text{for barriers} \\ 0 & \text{for wells.} \end{cases} \quad (3)$$

Here,  $v_F \approx 0.5 \times 10^6$  m/s is the Fermi velocity of the charge carriers in silicene,  $\vec{p} = (p_x, p_y)$  is the two-dimensional momentum,  $\vec{\sigma} = (\sigma_x, \sigma_y, \sigma_z)$  is the vector of Pauli matrices related to the sublattice pseudospin, and  $\Delta_{so}$  represents the spin-orbit interaction. In addition,  $s_z = \pm 1$  and  $\tau_z = \pm 1$  stand for the spin and valley indices, while  $\theta = \pm 1$  stands for the magnetization configuration. In the case of the AM configuration the magnetization of the second barrier in the superlattice unit cell is reversed ( $\theta = -1$ ).

To implement the transfer matrix method and with it obtain the transmission and transport properties of MSSSLs, it is necessary to know the wave functions and wave vectors in the different regions of the superlattice structure. We can know this information by solving the eigenvalue equation  $\hat{H}\psi = E\psi$ . In particular, the wave functions in the barrier regions are given as

$$\psi_{\pm}^b(x, y) = A_{\pm}^b \begin{pmatrix} 1 \\ v_{\pm}^b \end{pmatrix} e^{\pm i q_x^b x + i q_y^b y}, \quad (4)$$

with

$$v_{\pm}^b = \frac{\hbar v_F (\pm q_x^b - i \tau_z q_y^b)}{E + s_z \theta h - (\tau_z s_z \Delta_{so} - \Delta_z)} \quad (5)$$

and

$$q_x^b = \frac{1}{\hbar v_F} \sqrt{(E + s_z \theta h)^2 - (\tau_z s_z \Delta_{so} - \Delta_z)^2 - (\hbar v_F q_y^b)^2}. \quad (6)$$

In the case of the well regions, the wave functions and wave vector can be obtained straightforwardly by setting  $h = 0$ , and in the semi-infinite regions by setting  $\Delta_z = 0$  and  $h = 0$ . To identify the well region quantities, we use  $w$  as a superscript.

Now, we can relate the coefficients of the wave functions in the left semi-infinite region of our structure with the corresponding ones in the right semi-infinite region through the

transfer matrix of the superlattice structure. Namely,

$$\begin{pmatrix} A_+^L \\ A_-^L \end{pmatrix} = M^{SL} \begin{pmatrix} A_+^R \\ A_-^R \end{pmatrix}, \quad (7)$$

where

$$M^{SL} = [M_{uc}^{SL}]^N, \quad (8)$$

$M_{uc}^{SL}$  being the transfer matrix of the superlattice unit cell. Here, it is important to remark that we can define two unit cells within the superlattice unit cell, as we can appreciate in the exchange field profiles of Figs. 1(b) and 1(c). So, we can write  $M_{uc}^{SL}$  as

$$M_{uc}^{SL} = M_{uc1} M_{uc2}, \quad (9)$$

with  $M_{uc1}$  and  $M_{uc2}$  being the transfer matrix of the first and second unit cell of the superlattice unit cell, respectively. These matrices can be written in terms of the transfer matrices of the corresponding barrier and well regions

$$M_{uc1} = M_{b1} M_{w1}, \quad (10)$$

$$M_{uc2} = M_{b2} M_{w2}, \quad (11)$$

where

$$M_{b1} = D_0^{-1} (D_{b1} P_{b1} D_{b1}^{-1}) D_0, \quad (12)$$

$$M_{w1} = D_0^{-1} (D_{w1} P_{w1} D_{w1}^{-1}) D_0, \quad (13)$$

$$M_{b2} = D_0^{-1} (D_{b2} P_{b2} D_{b2}^{-1}) D_0, \quad (14)$$

$$M_{w2} = D_0^{-1} (D_{w2} P_{w2} D_{w2}^{-1}) D_0, \quad (15)$$

with  $D_0$ ,  $D_{b1}$ , and  $D_{b2}$  and  $P_{b1}$ ,  $P_{w1}$ ,  $P_{b2}$ , and  $P_{w2}$  being the so-called dynamic and propagation matrices. These matrices are given in terms of the wave function coefficients, wave vectors, and widths of the barrier and well regions. Explicitly,

$$D_i = \begin{pmatrix} 1 & 1 \\ v_+^i & v_-^i \end{pmatrix} \quad (16)$$

and

$$P_i = \begin{pmatrix} e^{-i q_i^i d_i} & 0 \\ 0 & e^{i q_i^i d_i} \end{pmatrix}, \quad (17)$$

where  $i = 0, b1, b2, w1, w2$  runs over the barrier and well regions. Here, it is important to remark that as the semi-infinite are identical, the dynamic matrices are the same,  $D_0$ . Similarly, as the wells are identical  $D_{w1} = D_{w2}$ .

The transmission probability or transmittance is defined in terms of the probability density fluxes

$$T_{\tau_z s_z}^{\theta_1 \theta_2} = \left| \frac{j_x^{\text{out}}}{j_x^{\text{in}}} \right|, \quad (18)$$

$j_x^{\text{in}}$  being the probability density flux associated with the incoming waves in the left semi-infinite region and  $j_x^{\text{out}}$  being that corresponding to the outgoing waves in the right semi-infinite region. By considering the  $x$  component of the probability density flux for Dirac electrons  $j_x = v_F \psi^\dagger \sigma_x \psi$  we can write the transmission in terms of the wave function

amplitudes of the incoming and outgoing waves as

$$T_{\tau_z s_z}^{\theta_1 \theta_2} = \frac{q_x^R [(E + s_z h_L \phi_L) - (\tau_z s_z \Delta_{so} - \Delta_z^L)] |A_+^R|^2}{q_x^L [(E + s_z h_R \phi_R) - (\tau_z s_z \Delta_{so} - \Delta_z^R)] |A_+^L|^2}. \quad (19)$$

This expression applies in general for superlattices in which the left and right semi-infinite regions are subjected to exchange and electric fields,  $\phi_L$  and  $\phi_R$  being the angles of the wave vectors  $q^L$  and  $q^R$  in those regions. However, in our case the semi-infinite regions are free, and then the transmission adopts the following form:

$$T_{\tau_z s_z}^{\theta_1 \theta_2} = \left| \frac{A_+^R}{A_+^L} \right|^2, \quad (20)$$

or according to Eq. (7),

$$T_{\tau_z s_z}^{\theta_1 \theta_2} = \left| \frac{1}{M_{11}^{SL}} \right|^2, \quad (21)$$

$M_{11}^{SL}$  being the (1,1) element of  $M^{SL}$ . We have labeled the transmission with the valley, spin, and magnetization configuration indices to identify the transmission components associated with a specific magnetization configuration as well as a specific valley-spin channel. In particular, we will identify PM when  $\theta_1 \theta_2 \rightarrow \uparrow \uparrow$  and AM when  $\theta_1 \theta_2 \rightarrow \uparrow \downarrow$ , the  $K$  and  $K'$  valley when  $\tau_z \rightarrow K$  and  $\tau_z \rightarrow K'$ , and spin up and spin down when  $s_z \rightarrow \uparrow$  and  $s_z \rightarrow \downarrow$ . For instance,  $T_{K \uparrow}^{\uparrow \uparrow}$  will be the transmission associated with the  $K$  valley and the spin-up component for the PM configuration.

The transport properties are obtained within the lines of the Landauer-Büttiker formalism. In specific, the spin-valley resolved conductance for a particular magnetization configuration at zero temperature is given as

$$G_{\tau_z s_z}^{\theta_1 \theta_2} = G_0 \int_{-\pi/2}^{\pi/2} T_{\tau_z s_z}^{\theta_1 \theta_2} \cos \phi d\phi, \quad (22)$$

where  $G_0 = e^2 L_y k_F / 2\pi h$  is the fundamental conductance factor. Here,  $L_y$  represents the width of the silicene sheet,  $k_F = \sqrt{E^2 - \Delta_{so}^2} / \hbar v_F$  represents the Fermi wave vector in the semi-infinite free regions, and  $\phi$  represents the angle of the impinging charge carriers.

The conductance allows us to compute the tunneling magnetoresistance (TMR) through the so-called total charge conductance

$$\text{TMR} = \frac{G_c^{\uparrow \uparrow} - G_c^{\downarrow \downarrow}}{G_c^{\uparrow \downarrow}}, \quad (23)$$

where  $G_c^{\uparrow \uparrow} = \sum_{\tau_z s_z} G_{\tau_z s_z}^{\uparrow \uparrow}$  ( $G_c^{\downarrow \downarrow} = \sum_{\tau_z s_z} G_{\tau_z s_z}^{\downarrow \downarrow}$ ) is the total charge conductance for the PM (AM) configuration.

Finally, the conductance spin-valley polarizations for the magnetization configurations are given as [31,73]

$$\eta_s^{\theta_1 \theta_2} = \frac{\sum_{\tau_z} (G_{\tau_z \uparrow}^{\theta_1 \theta_2} - G_{\tau_z \downarrow}^{\theta_1 \theta_2})}{\sum_{\tau_z s_z} G_{\tau_z s_z}^{\theta_1 \theta_2}} \quad (24)$$

and

$$\eta_v^{\theta_1 \theta_2} = \frac{\sum_{s_z} (G_{K s_z}^{\theta_1 \theta_2} - G_{K' s_z}^{\theta_1 \theta_2})}{\sum_{\tau_z s_z} G_{\tau_z s_z}^{\theta_1 \theta_2}}. \quad (25)$$

### III. RESULTS AND DISCUSSION

In this section we will analyze the main results of the magnetoresistance and spin-valley polarization of MSSLs. Firstly, we will show the results of symmetric MSSLs (S-MSSLs), that is, superlattices in which the structural parameters such as the widths of the barriers and wells as well as the strength of the external fields are the same. Secondly, we will address the so-called asymmetric MSSLs (A-MSSLs), that is, superlattices in which the structural parameters are dissimilar. In particular, we want to see whether structural asymmetry is helpful to improve the magnetoresistance and spin-valley polarization of MSSLs. Here, it is important to mention that we will focus on the variation in  $\Delta_z$  as a practical modulating parameter, keeping constant the energy of the charge carriers ( $E = 3.0 \Delta_{so}$ ) and the superlattice periods ( $N = 10$ ) throughout the analysis. In what follows, the energies and widths will be given in units of  $\Delta_{so}$  and  $l_{so} = \hbar v_F / \Delta_{so} = 89.6$  nm, respectively.

#### A. Symmetric MSSLs

First, we analyze the transmission characteristics of the charge carriers through S-MSSLs. In Fig. 2 we show the transmission maps as a function of  $\Delta_z$  and  $\phi$ . The first row of panels corresponds to PM, while the second row corresponds to AM. The width of barriers-wells and the strength of the exchange field are  $d_{B1} = d_{B2} = d_{W1} = d_{W2} = 2.0 l_{so}$  and  $h = 0.6 \Delta_{so}$ , respectively. As we can see, all transmission maps for PM are different, while for AM there is a symmetry between the transmission maps of spin-up (spin-down) electrons in the  $K$  valley and spin-down (spin-up) electrons in the  $K'$  valley. These characteristics are directly related to the distribution of Dirac cones along the superlattice axis according to the spin and valley as well as the magnetization configuration. In fact, the spin-valley distribution of Dirac cones for PM and AM is shown in Figs. 3 and 4, respectively. As we can notice, for PM the distribution is different for all spin-valley possibilities. In the case of AM, at first sight, the distribution is also different for all spin-valley components. However, if we look carefully, the distribution of Dirac cones for spin-up (spin-down) electrons in the  $K$  valley from right to left is the same as that corresponding to spin-down (spin-up) electrons from left to right. So, as the transmission properties are independent of whether electrons propagate from the left or from the right, the transmission map result is the same for spin-up (spin-down) electrons in the  $K$  valley and spin-down (spin-up) electrons in the  $K'$  valley. We can also see in all transmission maps semicircular regions with high and low transmission as a consequence of the periodic magnetic modulation. Moreover, we can notice that propagating modes dominate the transmission characteristics of spin-up (spin-down) electrons in the  $K$  ( $K'$ ) valley for both PM and AM, while evanescent modes shape to great extent the transmission characteristics of spin-down (spin-up) electrons in the  $K$  ( $K'$ ) valley for both magnetization configurations as well. In particular, in the latter case, the transmission is practically negligible for angles greater than  $\pm \pi/4$  and on-site potentials larger than  $\Delta_{so}$ , except for spin-up electrons in the  $K'$  valley for which the angular and on-site energy ranges are a bit larger. The



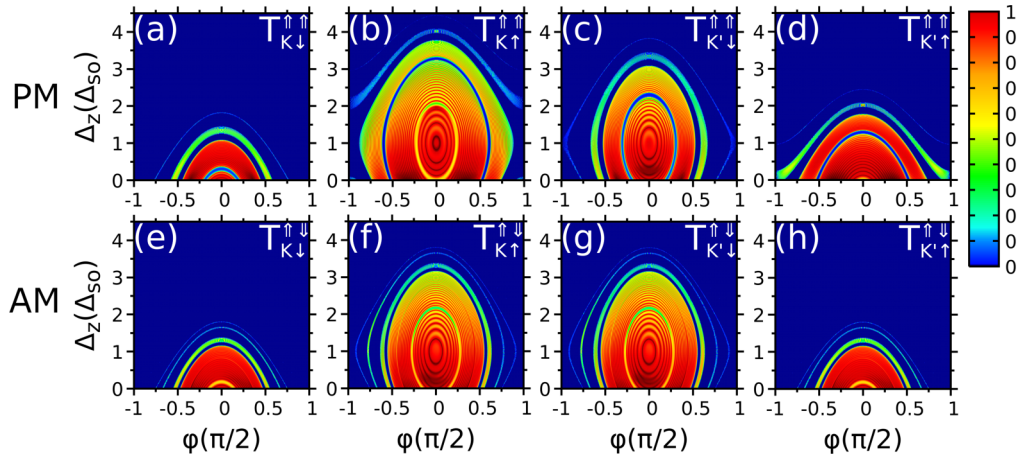


FIG. 2. Transmission maps as a function of the on-site potential energy  $\Delta_z$  and the angle of incidence  $\phi$  for S-MSSLs. (a)–(d) correspond to the transmission maps of the different spin-valley components for PM, while (e)–(h) correspond to the transmission maps of the spin-valley components for AM. The energy of the incident electron is  $E = 3.0\Delta_{so}$ , the width of barriers and wells is the same,  $d_{B1} = d_{B2} = d_{W1} = d_{W2} = 2.0l_{so}$ , the strength of the exchange field is  $h = 0.6\Delta_{so}$ , and the number of superlattice periods  $N = 10$ .

propagating or evanescent character of electrons is dictated by Eq. (6), in which the on-site potential, the angle of incidence, the spin-valley indices, and the magnetization configuration are involved. In particular, if the wave vector is real, we are dealing with propagating modes, while if it is pure imaginary, we are talking about evanescent modes. As we will see in short, all these characteristics of the transmission maps will be reflected in the conductance, spin-valley polarization, and magnetoresistance.

In Fig. 5 the spin-valley conductance of S-MSSLs for PM [Fig. 5(a)] and AM [Fig. 5(b)] is shown. The solid curves correspond to electrons in the  $K$  valley, while the dashed ones correspond to electrons in the  $K'$  valley. The superlattice parameters are the same as in Fig. 2. In correspondence with the characteristics of the transmission maps, the electronic transport is dominated by spin-valley electrons in which propagating modes are preponderant. Specifically, spin-up (spin-

down) electrons in the  $K$  ( $K'$ ) valley have a larger conductance for both magnetization configurations. This preponderance takes place for almost all on-site potential values considered, except for  $\Delta_z < \Delta_{so}$ , where spin-up electrons of the  $K'$  valley dominate over its spin-down counterparts. Furthermore, all spin-valley components of the conductance are different for PM, while for AM identical conductances are presented for spin-up (spin-down) electrons in the  $K$  valley and spin-down (spin-up) ones in the  $K'$  valley. The oscillating character of the conductance as a consequence of the periodic magnetic modulation is presented in all spin-valley components. In particular, the conductance as a function of  $\Delta_z$  presents two fundamental characteristics: descending envelopes with peaks inside them proportional to the number of wells in the structure. See, for instance,  $G_{K\uparrow}^{\uparrow\uparrow}$  and  $G_{K\uparrow}^{\uparrow\downarrow}$  in Figs. 6 and 7, respectively. More importantly, the periodic magnetic modulation creates on-site potential energy windows

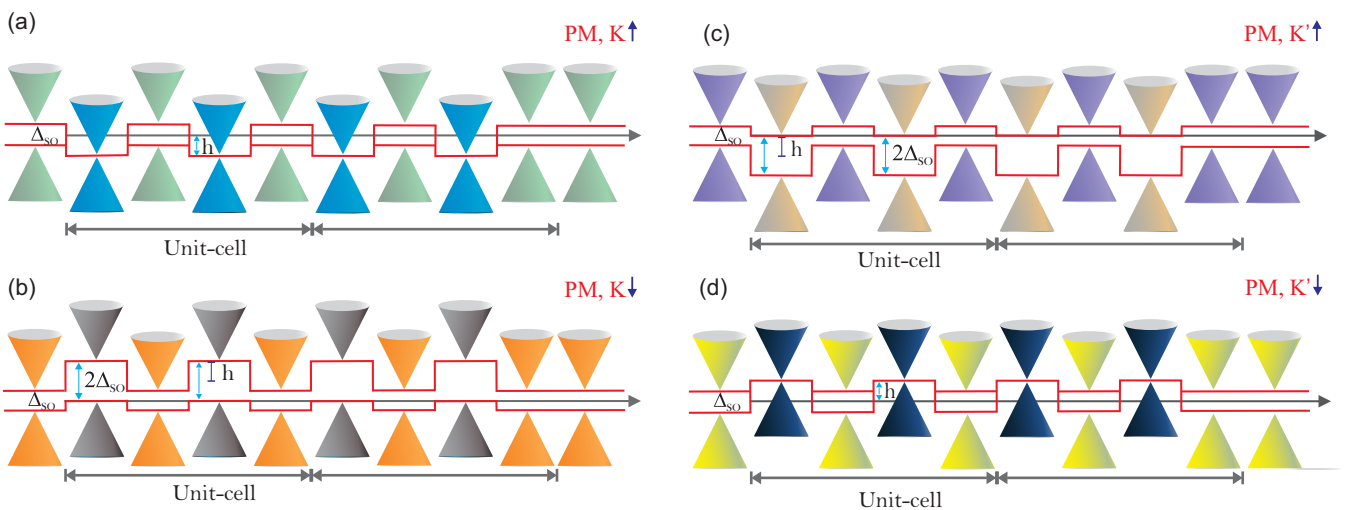


FIG. 3. (a)–(d) Distribution of Dirac cones along the superlattice axis for the different spin-valley components of the PM configuration of S-MSSLs. For this particular schematic representation,  $\Delta_z = 1.0\Delta_{so}$ ,  $h = 1.0\Delta_{so}$ , and  $N = 2$ . As can be seen, all Dirac cone distributions are different in the case of PM. The different colors highlight the mentioned difference.

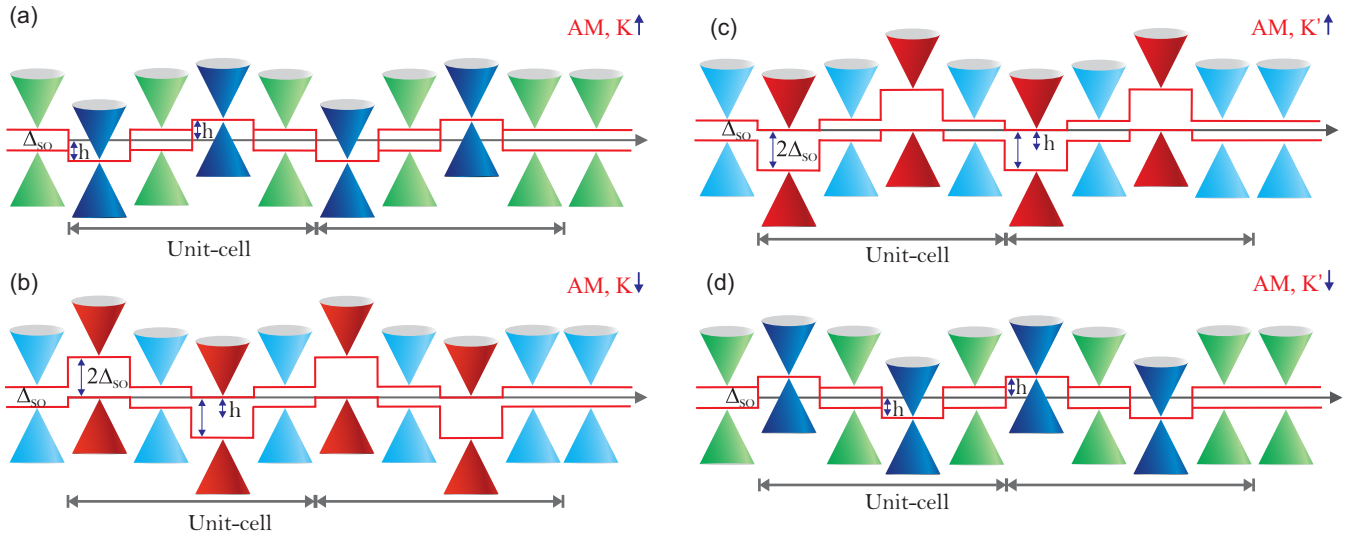


FIG. 4. (a)–(d) Distribution of Dirac cones along the superlattice axis for the different spin-valley components of the AM configuration of S-MSSLs. The parameters are the same as in Fig. 3. In this case, the Dirac cone distribution for spin-up (spin-down) electrons in the  $K$  valley is equivalent to that corresponding to spin-down (spin-up) electrons in the  $K'$  valley. The equivalence in the colors highlights the equivalence of the spin-valley components.

in which the spin-valley components of the conductance for PM are enhanced, while those corresponding to AM are diminished. This is quite evident for  $\Delta_z > 3.5\Delta_{so}$ , where the total conductance for AM has collapsed and that corresponding to PM is still significant; see the solid black and dashed blue curves in Fig. 8(a). This is in stark contrast to the conductance dynamics in single magnetic tunnel junctions [35], where the difference between the conductance of PM and AM is not as significant as for MSSLs. Regarding the TMR, what is fundamental is not only the difference between  $G_c^{\uparrow\uparrow}$  and  $G_c^{\downarrow\downarrow}$ , but also that  $G_c^{\downarrow\downarrow}$  be as low as possible. Actually, this combination takes place for  $3.2\Delta_{so} < \Delta_z < 3.8\Delta_{so}$ , as we can

appreciate in Fig. 8(a). In fact, it is in this on-site potential energy window that the TMR reaches its maximum values as shown in Fig. 9(a). The magnetoresistance also oscillates as a result of the periodic magnetic modulation. The descending envelopes and the peaks inside them are also presented in the TMR. In addition, at the start of each descending envelope an abrupt rise in the TMR takes place. These characteristics result in maximal TMR on the low-energy side of the descending envelopes. In particular, we can see two maxima associated with the oscillating magnetoresistance, one at about  $\Delta_z = 3.4\Delta_{so}$  and the other around  $\Delta_z = 3.65\Delta_{so}$ . The former is 2.4 times larger than the maximum value reported in single magnetic tunnel junctions for  $h = 0.6\Delta_{so}$  [35], while

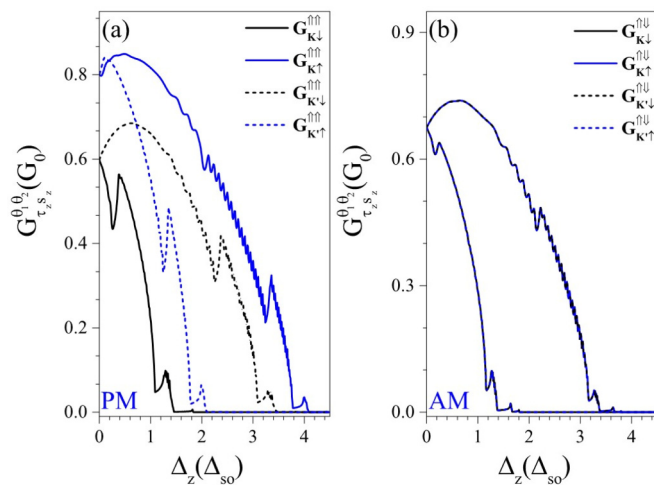


FIG. 5. Conductance as a function of  $\Delta_z$  for (a) PM and (b) AM configurations of S-MSSLs. The solid curves correspond to the conductance spin components in the  $K$  valley, while the dashed curves correspond to the conductance spin components in the  $K'$  valley. The superlattice parameters are the same as in Fig. 2.

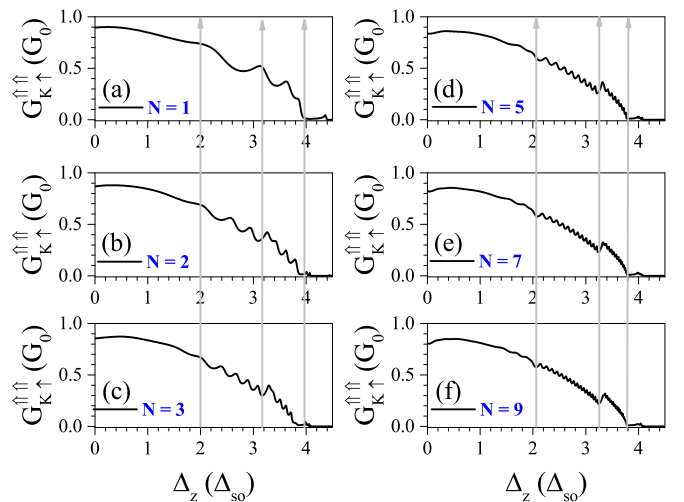


FIG. 6. (a)–(f) Conductance as a function of  $\Delta_z$  of S-MSSLs for different numbers of periods as indicated. All plots correspond to the spin-up component of the  $K$  valley for PM. The other superlattice parameters are the same as in Fig. 2.

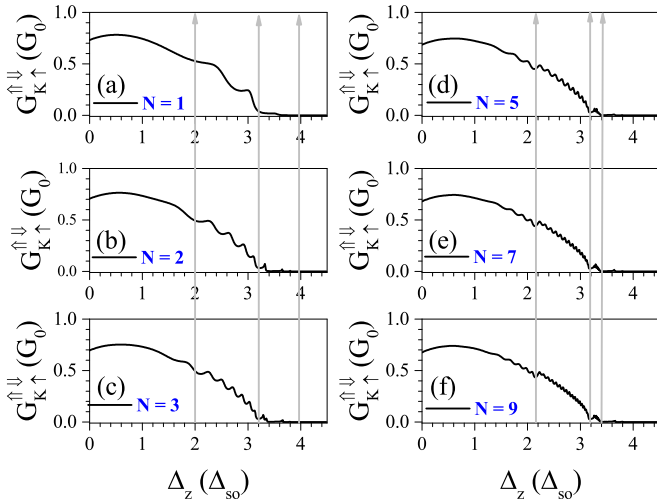


FIG. 7. (a)–(f) Same as Fig. 6, but for the AM configuration.

the latter is 4.8 times the maximum value mentioned for single magnetic tunnel junctions [35]. By increasing the strength of the exchange field it is possible to enhance the TMR. Specifically, if we increase the exchange field up to  $h = 1.2\Delta_{so}$ , the mentioned TMR maxima increase by almost an order of magnitude. This enhancement is 4.8 times greater than the maximum value reported for single magnetic tunnel junctions for the same exchange field strength [35]. The exchange field

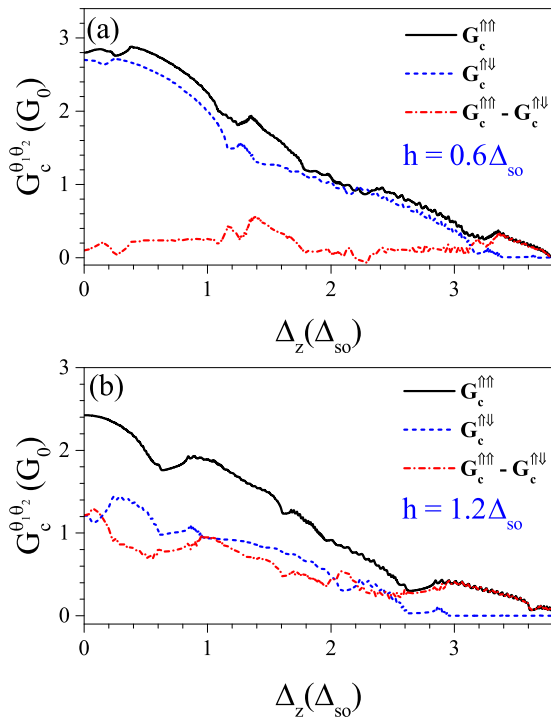


FIG. 8. (a) Total conductance as a function of  $\Delta_z$  for S-MSSLs with  $h = 0.6\Delta_{so}$ . The solid black, dashed blue, and dash-dotted red curves correspond to the total conductance for PM, the total conductance for AM, and the difference between both magnetization configurations, respectively. (b) Same as (a), but for  $h = 1.2\Delta_{so}$ . In both cases the other superlattice parameters are the same as in Fig. 2.

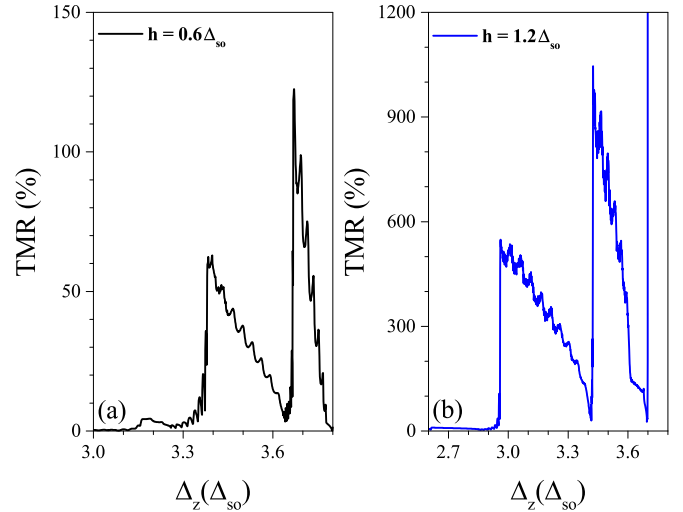


FIG. 9. TMR as a function of  $\Delta_z$  for S-MSSLs with (a)  $h = 0.6\Delta_{so}$  and (b)  $h = 1.2\Delta_{so}$ . In both cases the other superlattice parameters are the same as in Fig. 2.

increase also shifts the TMR maxima to lower on-site potential energies. In particular, the maxima are now located at about  $\Delta_z = 3.0\Delta_{so}$  and  $\Delta_z = 3.44\Delta_{so}$ . The enhancement and shift of the TMR maxima obey the enlargement of the on-site potential energy region, in which the combination of a significant difference between  $G_c^{\uparrow\uparrow}$  and  $G_c^{\uparrow\downarrow}$  and a low  $G_c^{\uparrow\downarrow}$  is taking place. In fact, this fundamental combination now is presented from  $\Delta_z = 2.6\Delta_{so}$  to  $\Delta_z = 3.9\Delta_{so}$ , as shown in Fig. 8(b).

To end this section, we analyze the impact of the periodic magnetic modulation on the spin-valley polarization. In Fig. 10 we show the spin [Fig. 10(a)] and valley [Fig. 10(b)] polarization for the PM configuration of S-MSSLs. The solid black and solid blue curves correspond to exchange field

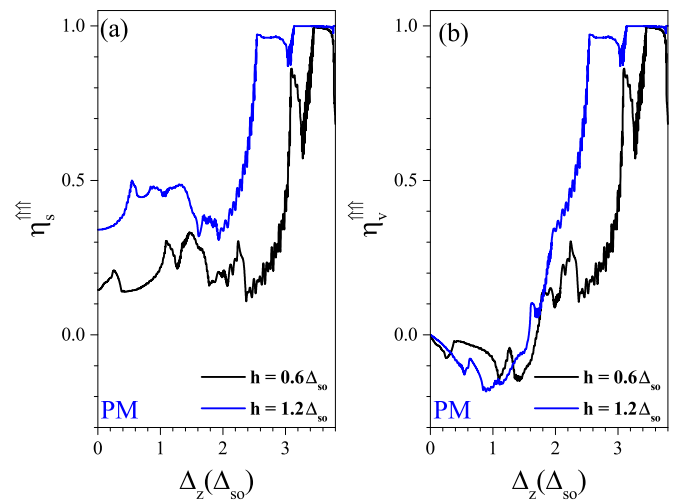


FIG. 10. (a) Spin and (b) valley polarization as a function of  $\Delta_z$  for S-MSSLs. The solid black curves correspond to  $h = 0.6\Delta_{so}$ , while the solid blue curves correspond to  $h = 1.2\Delta_{so}$ . For both polarizations the other superlattice parameters are the same as in the preceding figures.

strengths  $h = 0.6\Delta_{so}$  and  $h = 1.2\Delta_{so}$ , respectively. As we can notice, the spin-valley polarization also presents oscillations as a result of the periodic magnetic modulation. The oscillations are more pronounced for  $h = 0.6\Delta_{so}$ . Furthermore, the degree of spin-valley polarization is low at small on-site potential energies and is enhanced as the on-site potential energy increases, reaching full polarization after  $\Delta_z = 3.5\Delta_{so}$  ( $\Delta_z = 2.6\Delta_{so}$ ) for  $h = 0.6\Delta_{so}$  ( $h = 1.2\Delta_{so}$ ). Actually, the full polarization region for  $h = 0.6\Delta_{so}$  is practically the same as for single magnetic tunnel junctions [35]. However, the periodic magnetic modulation gives us the possibility to increase the full polarization region by increasing the exchange field strength. In the case of single magnetic tunnel junctions the full polarization region remains practically the same regardless of the exchange field strength [35]. Regarding AM, the symmetry between spin-up (spin-down) electrons of the  $K$  valley and spin-down (spin-up) electrons of the  $K'$  valley impedes any spin-valley polarization. This can be seen straightforwardly from Eqs. (24) and (25), in which the equivalence between the spin-valley components of the conductance  $G_{K\uparrow}^{\uparrow\downarrow} = G_{K'\downarrow}^{\uparrow\downarrow}$  and  $G_{K\downarrow}^{\uparrow\downarrow} = G_{K'\uparrow}^{\uparrow\downarrow}$  results in null spin-valley polarization  $\eta_s^{\uparrow\downarrow} = \eta_v^{\uparrow\downarrow} = 0$ . So, the price to pay for the enhancement of the magnetoresistance through periodic magnetic modulation is the lack of two well-defined spin-valley polarization states. Specifically, in the case of S-MSSLs it is not possible to switch the state of spin-valley polarization by simply changing the magnetization configuration from PM to AM. This contrasts with single magnetic tunnel junctions, in which two well-defined spin-valley polarization states can be reached by simply reversing the magnetization configuration [35]. Actually, we can also obtain two well-defined spin-valley polarization states by reversing the magnetization of both barriers in the unit cell; see Figs. 11(a) and 11(b). However, there is no magnetoresistive response due to the equivalence between  $G_c^{\uparrow\uparrow}$  and  $G_c^{\downarrow\downarrow}$  as shown in Fig. 11(c). In fact, this is essentially what happens in most silicene superlattices [44,46,59], which are good spin-valley polarizers but poor magnetoresistive response systems. To overcome this obstacle and be able to obtain MSSLs with magnetoresistive and spin-valley polarization capabilities, we envisage two possibilities: (1) considering other distributions of Dirac cones, such as periodic arrangements with defects and/or aperiodic (Fibonacci, Thue-Morse, etc.) ones, and (2) changing the resonant conditions of the superlattice structure by inducing asymmetries through differentiating the width of barriers-wells and/or the strength of the exchange field between barriers. We will opt for the latter because the former requires a thorough assessment that goes beyond the aim of the present study.

### B. Asymmetric MSSLs

Here, we will analyze the impact of the structural asymmetry on the transport, magnetoresistance, and spin-valley polarization of MSSLs. In particular, we analyze the consequences of having barriers-wells of different width. In Fig. 12 we show the transmission maps as a function of  $\Delta_z$  for the different spin-valley components of A-MSSLs. The first row of panels corresponds to PM, while the second row corresponds to AM. The widths considered for the barriers and wells that

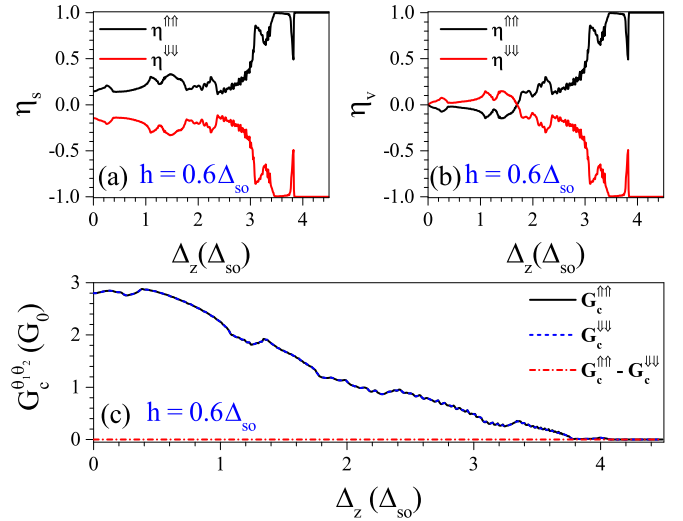


FIG. 11. (a) Spin and (b) valley polarization, and (c) total conductance as a function of  $\Delta_z$  for S-MSSLs in which all magnetic barriers are inverted in the AM configuration. As we can notice, an effective spin-valley polarization takes place for AM. However, the PM and AM conductances are the same, resulting in null TMR. The exchange field considered is  $h = 0.6\Delta_{so}$ . The other superlattice parameters are the same as in the preceding figures.

constitute the unit cell are  $d_{B1} = 3.0l_{so}$ ,  $d_{W1} = 1.0l_{so}$ ,  $d_{B2} = 2.0l_{so}$ , and  $d_{W2} = 2.0l_{so}$ , while the strength of the exchange field in the barriers is  $h = 0.6\Delta_{so}$ . As in the case of S-MSSLs the transmission characteristics are dominated by spin-up and spin-down electrons in the  $K$  and  $K'$  valley, respectively. However, as we can notice, practically all the transmission maps for both PM and AM are different. This is a good sign because in principle we can have spin-valley polarization for both magnetization configurations. Now, the matter is to see whether the magnetoresistance is preserved or not under the influence of the structural asymmetry induced by the width of barriers-wells. In Fig. 13 the different spin-valley components of the conductance for PM [Fig. 13(a)] and AM [Fig. 13(b)] are shown. As we can see, the structural asymmetry intensifies the oscillating character of the conductance. Also still evident is the difference between the spin-valley components of the conductance between PM and AM, which allows us to think about a good magnetoresistance response. More importantly, we can see a difference between the spin-valley components of the conductance for AM. Actually, the difference is not as significant as for PM, but at least the structural asymmetry can give us some on-site potential energy windows in which it is possible to achieve good spin-valley polarization characteristics. In Fig. 14 the total conductance of A-MSSLs for  $h = 0.6\Delta_{so}$  [Fig. 14(a)] and  $h = 1.2\Delta_{so}$  [Fig. 14(b)] is presented. The solid black, dashed blue, and dash-dotted red curves correspond to the conductance for PM, the conductance for AM, and the difference between the magnetization configurations, respectively. As we can see, the on-site potential energy window in which there is a significant difference between  $G_c^{\uparrow\uparrow}$  and  $G_c^{\downarrow\downarrow}$  as well as a diminished  $G_c^{\downarrow\downarrow}$  takes place from  $\Delta_z = 3.2\Delta_{so}$  to  $\Delta_z = 3.8\Delta_{so}$  for  $h = 0.6\Delta_{so}$ . If we increase the exchange field strength to  $h = 1.2\Delta_{so}$ , the on-site potential energy window enlarges, taking place now from  $\Delta_z = 2.3\Delta_{so}$



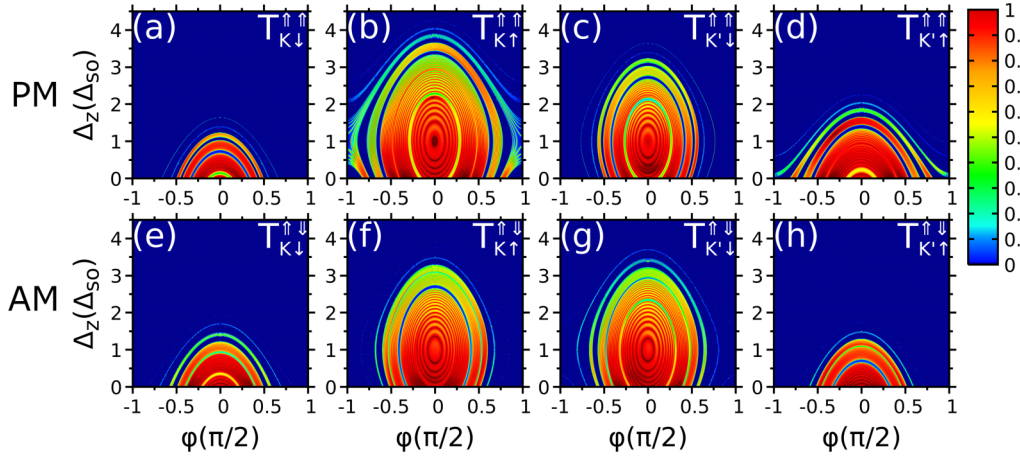


FIG. 12. Transmission maps as a function of  $\Delta_z$  and  $\phi$  for A-MSSLs. (a)–(d) correspond to the transmission maps of the different spin-valley components for the PM configuration, while (e)–(h) correspond to the transmission maps of the spin-valley components for the AM configuration. Here, the asymmetry is induced by considering different widths for barriers and wells:  $d_{B1} = 3.0l_{so}$ ,  $d_{B2} = 2.0l_{so}$ ,  $d_{W1} = 1.0l_{so}$ , and  $d_{W2} = 2.0l_{so}$ . The exchange field strength and the number of superlattice periods are  $h = 0.6\Delta_{so}$  and  $N = 10$ , respectively.

to  $\Delta_z = 4.0\Delta_{so}$ . This energy window is fundamental because in it we can have a significant magnetoresistance as well as a high degree of spin-valley polarization.

The impact of the structural asymmetry on the TMR is presented in Fig. 15. As we can note, the modification of the resonant conditions owing to the structural asymmetry shifts the TMR maxima to higher on-site potential energies and more importantly enhances significantly the TMR with respect to S-MSSLs. For instance, in the case of  $h = 0.6\Delta_{so}$ , the TMR maxima are now located at about  $\Delta_z = 3.5\Delta_{so}$  and  $\Delta_z = 3.71\Delta_{so}$  and have increased 2.93 and 1.64 times with respect to the corresponding ones of S-MSSLs. For  $h = 1.2\Delta_{so}$  the maxima have moved to  $\Delta_z = 3.2\Delta_{so}$  and  $\Delta_z = 3.6\Delta_{so}$  with enhancements of 4.6 and more than an order of

magnitude with respect to S-MSSLs, respectively. It is also important to remark that in comparison with single magnetic tunnel junctions the TMR of A-MSSLs is enhanced five times and more than an order of magnitude for  $h = 0.6\Delta_{so}$  and  $h = 1.2\Delta_{so}$ , respectively. So, these results indicate that the structural asymmetry related to the width of barriers-wells could be

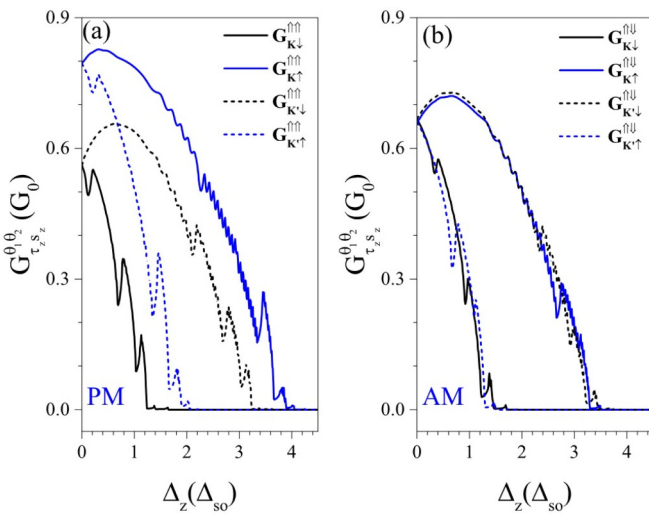


FIG. 13. Conductance as a function of the on-site potential energy for (a) PM and (b) AM configurations of A-MSSLs. The solid curves correspond to the conductance spin components in the  $K$  valley, while the dashed curves correspond to the conductance spin components in the  $K'$  valley. The superlattice structural parameters are the same as in Fig. 12.

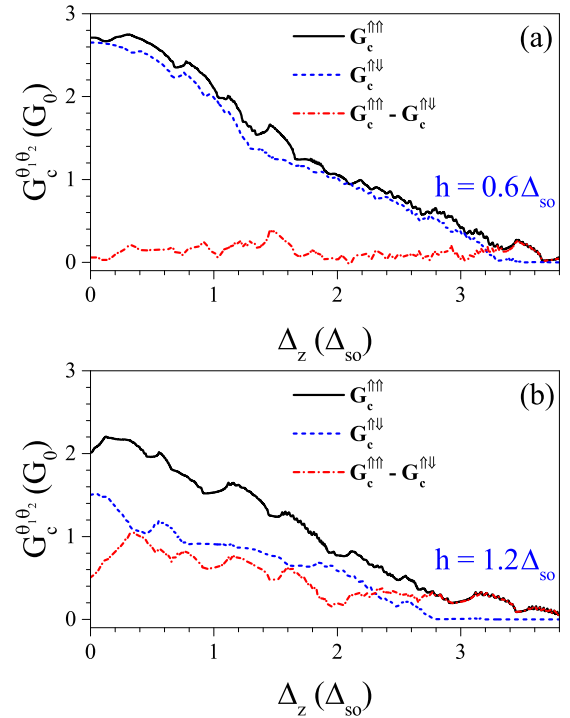


FIG. 14. (a) Total conductance as a function of  $\Delta_z$  for the magnetization configurations of A-MSSLs with  $h = 0.6\Delta_{so}$ . The solid black, dashed blue, and dash-dotted red curves correspond to the total conductance for PM, the total conductance for AM, and the difference between the magnetization configurations, respectively. (b) Same as (a), but for  $h = 1.2\Delta_{so}$ . In both cases the other superlattice parameters are the same as in the preceding figures.

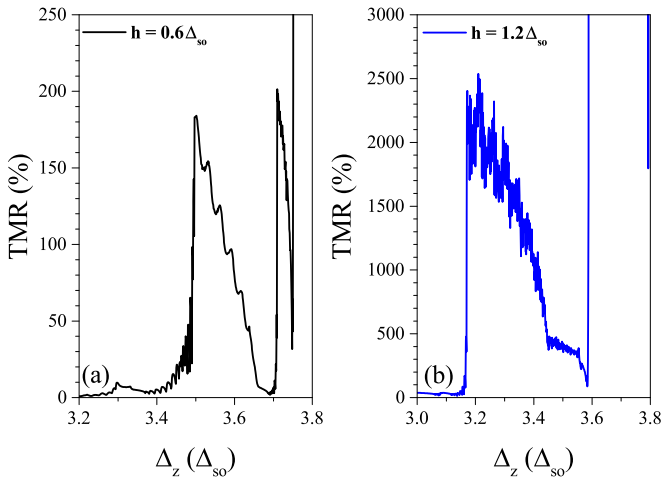


FIG. 15. TMR as a function of  $\Delta_z$  for A-MSSLs. The solid black and solid blue curves correspond to exchange field strengths of (a)  $h = 0.6\Delta_{so}$  and (b)  $h = 1.2\Delta_{so}$ , respectively. The other superlattice parameters are the same as in the preceding figures.

a good option to improve the TMR response of MSSLs. Now, the matter is to see whether it also works appropriately to provide effective spin-valley polarization. In Fig. 16 we show the spin-valley polarization as a function of  $\Delta_z$  for A-MSSLs. Figures 16(a) and 16(b) correspond to the spin and valley polarization for  $h = 0.6\Delta_{so}$ , while Figs. 16(c) and 16(d) correspond to the spin and valley polarization for  $h = 1.2\Delta_{so}$ . The solid black and solid blue curves correspond to PM and AM, respectively. As in the case of S-MSSLs, the significant differentiation between the spin-valley components of the conductance for PM gives rise to well-defined spin-valley polarization. As we can see, the degree of spin-valley polarization is low or practically zero at small on-site potential energies. As the on-site potential energy increases, the spin-

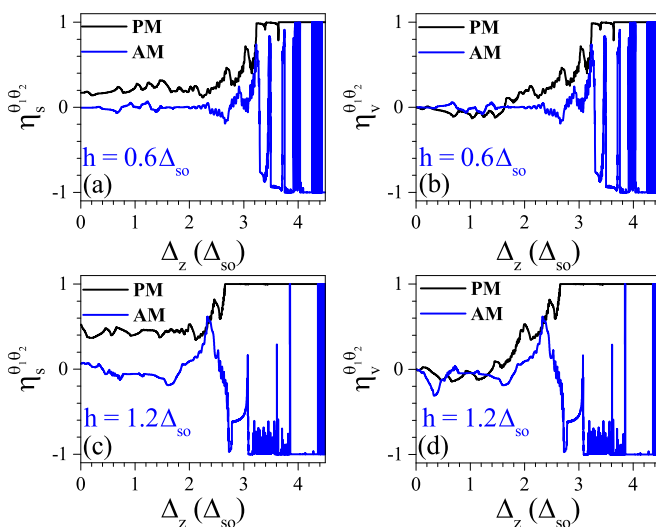


FIG. 16. (a) Valley and (b) spin polarization as a function of  $\Delta_z$  for A-MSSLs with  $h = 0.6\Delta_{so}$ . The solid black curves correspond to PM, while the solid blue curves correspond to AM. (c) and (d) are the same as (a) and (b), respectively, but for  $h = 1.2\Delta_{so}$ . In all cases the superlattice parameters are the same as in the preceding figures.

valley polarization increases as well, reaching 100% positive polarization after  $\Delta_z = 3.3\Delta_{so}$  ( $\Delta_z = 2.7\Delta_{so}$ ) for  $h = 0.6\Delta_{so}$  ( $h = 1.2\Delta_{so}$ ). The spin-valley polarization also shows oscillations as a consequence of the periodic magnetic modulation. In general, we can appreciate an effective improvement in the spin-valley polarization owing to the structural asymmetry associated with the width of barriers-wells. Specifically, the flatness of the polarization regions is superior in A-MSSLs compared with S-MSSLs. Moreover, the spin polarization of A-MSSLs, in contrast to S-MSSLs, is 25% in the range  $0.0\Delta_{so} < \Delta_z < 3.0\Delta_{so}$  for  $h = 0.6\Delta_{so}$ , increasing up to 50% for  $h = 1.2\Delta_{so}$  in the range  $0.0\Delta_{so} < \Delta_z < 2.5\Delta_{so}$ . In the case of AM, the impact of the structural asymmetry of the width of barriers-wells is remarkable. In fact, the structural asymmetry creates on-site potential energy windows with 100% or almost 100% negative spin-valley polarization alternating with narrow energy windows of a high degree of (almost 100%) positive spin-valley polarization. This alternate dynamic is reduced as the strength of the exchange field increases. In particular, we find five alternate regions for  $h = 0.6\Delta_{so}$  and three regions for  $h = 1.2\Delta_{so}$ . These results are quite interesting because in principle it is possible to have two well-defined polarization states by fixing the on-site potential energy and changing the magnetization configuration or by fixing the magnetization configuration to AM and adjusting the on-site potential energy. In the latter case, it is fundamental to have a high degree of control in the tuning of  $\Delta_z$  due to the narrowness of the positive polarization regions.

#### IV. CONCLUSIONS

In summary, we showed that the TMR and spin-valley polarization in silicene can be improved by FMEs arranged in periodic fashion. We have considered superlattices with two FMEs and two free regions as the unit cell. The second FME plays the role of soft region, allowing us to change from PM to AM configuration by reversing its magnetization direction. A metallic electrode along the superlattice structure and underneath FMEs is used to modulate the silicene on-site potential (local band gap) through an applied perpendicular electric field. We have used a low-energy effective Hamiltonian to describe the charge carriers in silicene. The well-known transfer matrix method and the Landauer-Büttiker formalism were implemented to obtain the transmission and transport properties, respectively. We found that once the periodic modulation is incorporated, the conductance oscillates and the AM component of it diminishes significantly, resulting in an effective improvement in the TMR. In particular, the magnetoresistance can be enhanced five times with respect to single magnetic barriers. In the case of spin-valley polarization it is necessary to induce structural asymmetry in the superlattice to obtain two well-defined polarization states with a high degree of polarization. Moreover, we can switch the polarization states by simply changing the magnetization configuration. The structural asymmetry also induced a further enhancement of the TMR, more than an order of magnitude with respect to single magnetic junctions. Our findings indicate that MSSLs can be useful for versatile devices with magnetoresistive and spin-valley polarization capabilities. Finally, it is important to remark that structural disorder [74,75], temperature [61],

and noncollinear magnetization [76,77] effects could affect the magnetoresistive response and the spin-valley polarization of MSSLs; consequently, a thorough analysis of these effects is needed.

## ACKNOWLEDGMENT

The authors acknowledge CONACYT-Mexico for its support in the development of the present work through Grant No. A1-S-11655.

- 
- [1] E. C. Ahn, *npj 2D Mater. Appl.* **4**, 17 (2020).
- [2] A. Avsar, H. Ochoa, F. Guinea, B. Özyilmaz, B. J. van Wees, and I. J. Vera-Marun, *Rev. Mod. Phys.* **92**, 021003 (2020).
- [3] J. R. Schaibley, H. Yu, G. Clark, P. Rivera, J. S. Ross, K. L. Seyler, W. Yao, and X. Xu, *Nat. Rev. Mater.* **1**, 16055 (2016).
- [4] M. Drögel, C. Franzen, F. Volmer, T. Pohlmann, L. Banszerus, M. Wolter, K. Watanabe, T. Taniguchi, C. Stampfer, and B. Beschoten, *Nano Lett.* **16**, 3533 (2016).
- [5] J. Ingla-Aynés, R. J. Meijerink, and B. J. van Wees, *Nano Lett.* **16**, 4825 (2016).
- [6] N. Tombros, C. Jozsa, M. Popinciuc, H. T. Jonkman, and B. J. van Wees, *Nature (London)* **448**, 571 (2007).
- [7] A. L. Friedman, O. M. van't Erve, C. H. Li, J. T. Robinson, and B. T. Jonker, *Nat. Commun.* **5**, 3161 (2014).
- [8] T. Cao, G. Wang, W. Han, H. Ye, C. Zhu, J. Shi, Q. Niu, P. Tan, E. Wang, B. Liu, and J. Feng, *Nat. Commun.* **3**, 887 (2012).
- [9] H. Zeng, J. Dai, W. Yao, D. Xiao, and X. Cui, *Nat. Nanotechnol.* **7**, 490 (2012).
- [10] K. F. Mak, K. He, J. Shan, and T. F. Heinz, *Nat. Nanotechnol.* **7**, 492 (2012).
- [11] J. Lee, K. F. Mak, and J. Shan, *Nat. Nanotechnol.* **11**, 421 (2016).
- [12] T. Y. Hung, K. Y. Camsari, S. Zhang, P. Upadhyaya, and Z. Chen, *Sci. Adv.* **5**, eaau6478 (2019).
- [13] Y. Wu, G. Yin, L. Pan, A. J. Grutter, Q. Pan, A. Lee, D. A. Gilbert, J. A. Borchers, W. Ratcliff II, A. Li, X.-D. Han, and K. L. Wang, *Nat. Electron.* **3**, 604 (2020).
- [14] S. Cahangirov, M. Topsakal, E. Aktürk, H. Şahin, and S. Ciraci, *Phys. Rev. Lett.* **102**, 236804 (2009).
- [15] A. Kara, H. Enriquez, A. P. Seitsonen, L. C. L. Y. Voon, S. Vizzini, B. Aufray, and H. Oughaddou, *Surf. Sci. Rep.* **67**, 1 (2012).
- [16] J. Zhao, H. Liu, Z. Yu, R. Quhe, S. Zhou, Y. Wang, C. C. Liu, H. Zhong, N. Han, J. Lu, Y. Yao, and K. Wu, *Prog. Mater. Sci.* **83**, 24 (2016).
- [17] C.-C. Liu, W. Feng, and Y. Yao, *Phys. Rev. Lett.* **107**, 076802 (2011).
- [18] C.-C. Liu, H. Jiang, and Y. Yao, *Phys. Rev. B* **84**, 195430 (2011).
- [19] N. D. Drummond, V. Zólyomi, and V. I. Fal'ko, *Phys. Rev. B* **85**, 075423 (2012).
- [20] Z. Ni, Q. Liu, K. Tang, J. Zheng, J. Zhou, R. Qin, Z. Gao, D. Yu, and J. Lu, *Nano Lett.* **12**, 113 (2012).
- [21] P. Vogt, P. De Padova, C. Quaresima, J. Avila, E. Frantzeskakis, M. C. Asensio, A. Resta, B. Ealet, and G. Le Lay, *Phys. Rev. Lett.* **108**, 155501 (2012).
- [22] A. Florence, R. Friedlein, T. Ozaki, H. Kawai, Y. Wang, and Y. Yamada-Takamura, *Phys. Rev. Lett.* **108**, 245501 (2012).
- [23] L. Meng, Y. Wang, L. Zhang, S. Du, R. Wu, L. Li, Y. Zhang, G. Li, H. Zhou, W. A. Hofer, and H.-J. Gao, *Nano Lett.* **13**, 685 (2013).
- [24] L. Tao, E. Cinquanta, D. Chiappe, C. Grazianetti, M. Fanciulli, M. Dubey, A. Molle, and D. Akinwande, *Nat. Nanotechnol.* **10**, 227 (2015).
- [25] M. Ezawa, *Phys. Rev. Lett.* **109**, 055502 (2012).
- [26] H. Pan, Z. Li, C.-C. Liu, G. Zhu, Z. Qiao, and Y. Yao, *Phys. Rev. Lett.* **112**, 106802 (2014).
- [27] J. Linder and T. Yokoyama, *Phys. Rev. B* **89**, 020504(R) (2014).
- [28] X. Zhai, S. Zhang, Y. Zhao, X. Zhang, and Z. Yang, *Appl. Phys. Lett.* **109**, 122404 (2016).
- [29] I. Appelbaum, B. Huang, and D. J. Monsma, *Nature (London)* **447**, 295 (2007).
- [30] B. Huang, D. J. Monsma, and I. Appelbaum, *Phys. Rev. Lett.* **99**, 177209 (2007).
- [31] T. Fujita, M. B. A. Jalil, and S. G. Tan, *Appl. Phys. Lett.* **97**, 043508 (2010).
- [32] S. Wang, P. Zhang, C. Ren, H. Tian, J. Pang, C. Song, and M. Sun, *J. Supercond. Novel Magn.* **32**, 2947 (2019).
- [33] C. Xu, G. Luo, Q. Liu, J. Zheng, Z. Zhang, S. Nagase, Z. Gao, and J. Lu, *Nanoscale* **4**, 3111 (2012).
- [34] Y. Wang and Y. Lou, *J. Appl. Phys. (Melville, NY)* **114**, 183712 (2013).
- [35] D. Wang, Z. Huang, Y. Zhang, and G. Jin, *Phys. Rev. B* **93**, 195425 (2016).
- [36] D. Wang and G. Jin, *Phys. Lett. A* **378**, 2557 (2014).
- [37] S. Rachel and M. Ezawa, *Phys. Rev. B* **89**, 195303 (2014).
- [38] R. Saxena, A. Saha, and S. Rao, *Phys. Rev. B* **92**, 245412 (2015).
- [39] W.-F. Tsai, C.-Y. Huang, T.-R. Chang, H. Lin, H.-T. Jeng, and A. Bansil, *Nat. Commun.* **4**, 1500 (2013).
- [40] V. Vargiamidis and P. Vasilopoulos, *Appl. Phys. Lett.* **105**, 223105 (2014).
- [41] Y. Wang and Y. Lou, *Phys. Lett. A* **378**, 2627 (2014).
- [42] X. Zhai and G. Jin, *J. Phys.: Condens. Matter* **28**, 355002 (2016).
- [43] Y. Zhang and Y. Guo, *Eur. Phys. J. B* **90**, 27 (2017).
- [44] Q. Zhang, K. S. Chan, and J. Li, *Sci. Rep.* **6**, 33701 (2016).
- [45] W. Li, W.-T. Lu, Y.-F. Li, and H.-H. Han, *Phys. E (Amsterdam)* **88**, 284 (2017).
- [46] W.-T. Lu, Y.-F. Li, and H.-Y. Tian, *Nanoscale Res. Lett.* **13**, 84 (2018).
- [47] C. Yesilyurt, S. G. Tan, G. Liang, and M. B. A. Jalil, *Appl. Phys. Express* **8**, 105201 (2015).
- [48] M. Farokhnezhad, M. Esmaeilzadeh, and K. Shakouri, *Phys. Rev. B* **96**, 205416 (2017).
- [49] S.-K. Wang and J. Wang, *Chin. Phys. B* **24**, 037202 (2015).
- [50] S. Mirershadi and F. Sattari, *Phys. E (Amsterdam)* **115**, 113696 (2020).
- [51] H.-H. Shao, D. Guo, B.-L. Zhou, and G.-H. Zhou, *Chin. Phys. B* **25**, 037309 (2016).
- [52] J.-L. Zhang, W. Fu, K.-Y. Wang, S.-S. Ke, and H.-F. Lü, *Phys. B (Amsterdam)* **525**, 16 (2017).

- [53] F. Sattari and S. Mirershadi, *Phys. E (Amsterdam)* **124**, 114287 (2020).
- [54] T. Yokoyama, *Phys. Rev. B* **87**, 241409(R) (2013).
- [55] B. Soodchomshom, *J. Appl. Phys. (Melville, NY)* **115**, 023706 (2014).
- [56] Y. Wang, *Appl. Phys. Lett.* **104**, 032105 (2014).
- [57] V. Vargiamidis and P. Vasilopoulos, *J. Appl. Phys. (Melville, NY)* **117**, 094305 (2015).
- [58] Q. Zhang, K. S. Chan, and M. Long, *J. Phys.: Condens. Matter* **28**, 055301 (2016).
- [59] N. Missault, P. Vasilopoulos, V. Vargiamidis, F. M. Peeters, and B. Van Duppen, *Phys. Rev. B* **92**, 195423 (2015).
- [60] Z. P. Niu, Y. M. Zhang, and S. Dong, *New J. Phys.* **17**, 073026 (2015).
- [61] N. Missault, P. Vasilopoulos, F. M. Peeters, and B. Van Duppen, *Phys. Rev. B* **93**, 125425 (2016).
- [62] Z. Rashidian, Z. Lorestaniweiss, Y. Hajati, S. Rezaeipour, and G. Rashedi, *J. Magn. Magn. Mater.* **442**, 15 (2017).
- [63] Z. Rashidian, Y. Hajati, S. Rezaeipour, and S. Baher, *Phys. E (Amsterdam)* **86**, 111 (2017).
- [64] L.-L. Chang, Q.-P. Wu, R.-L. Zhang, Y.-Z. Li, M.-R. Liu, X.-B. Xiao, and Z.-F. Liu, *Phys. B (Amsterdam)* **601**, 412552 (2021).
- [65] X.-T. An, *Phys. Lett. A* **379**, 723 (2015).
- [66] X. Zhai, J. Gu, R. Wen, R.-W. Liu, M. Zhu, X. Zhou, L.-Y. Gong, and X. Li, *Phys. Rev. B* **99**, 085421 (2019).
- [67] F. Sattari and S. Mirershadi, *Eur. Phys. J. B* **91**, 259 (2018).
- [68] O. Oubram, O. Navarro, E. J. Guzmán, and I. Rodríguez-Vargas, *Superlattices Microstruct.* **113**, 483 (2018).
- [69] J. C. Egues, *Phys. Rev. Lett.* **80**, 4578 (1998).
- [70] D. Jin, Y. Ren, Z.-Z. Li, M.-W. Xiao, G. Jin, and A. Hu, *Phys. Rev. B* **73**, 012414 (2006).
- [71] H. Haugen, D. Huertas-Hernando, and A. Brataas, *Phys. Rev. B* **77**, 115406 (2008).
- [72] A. Yamakage, M. Ezawa, Y. Tanaka, and N. Nagaosa, *Phys. Rev. B* **88**, 085322 (2013).
- [73] V. H. Nguyen, A. Bournel, and P. Dollfus, *J. Appl. Phys. (Melville, NY)* **109**, 073717 (2011).
- [74] A. Esmailpour, M. Abdolmaleki, and M. Saadat, *Phys. E (Amsterdam)* **77**, 144 (2016).
- [75] O. Oubram, O. Navarro, E. J. Guzmán, and I. Rodríguez-Vargas, *Phys. E (Amsterdam)* **120**, 114100 (2020).
- [76] T. Yokoyama and J. Linder, *Phys. Rev. B* **83**, 081418(R) (2011).
- [77] M. Zare, L. Majidi, and R. Asgari, *Phys. Rev. B* **95**, 115426 (2017).